UNIVERSITY OF
BATH

Link to publication

University of Bath

Dynamical response and instability in ceria under lattice expansion

J. Buckeridge,[1,*] D. O. Scanlon,[1] A. Walsh,[2] C. R. A. Catlow,[1] and A. A. Sokol[1]

[1]*University College London, Kathleen Lonsdale Materials Chemistry, Department of Chemistry, 20 Gordon Street,
London WC1H 0AJ, United Kingdom*

[2]*Centre for Sustainable Chemical Technologies and Department of Chemistry, University of Bath, Claverton Down,
Bath BA2 7AY, United Kingdom*

We present results of density functional theory calculations on the phonon dispersion and elastic constants of bulk ceria (CeO_2) as a function of positive and negative isotropic strain, which could be induced thermally or by cationic doping. We find that, as the lattice is expanded, there is a significant softening of the B_{1u} mode at the X point. This mode consists of motions of oxygens in the [001] direction. At a strain of 1.6%, corresponding to a temperature of 1600 K, the B_{1u} and E_u modes at the X point cross, with an associated high, narrow peak in the phonon density of states appearing. We infer that this crossing indicates a coupling of the modes, leading to a transition to a superionic phase, where conductivity occurs in the [001] direction, mediated by anion interstitial site occupation. As the lattice is expanded further, the B_{1u} mode continues to soften, becoming imaginary at a strain of 3.4%, corresponding to a temperature of 2500 K. Following the imaginary mode would result in a cubic to tetragonal phase transition, similar to those known to occur with reducing temperature in zirconia (ZrO_2) and hafnia (HfO_2). Our calculated elastic constants, however, indicate that the structure remains mechanically stable, even at this level of expansion. As confirmed by our semiclassical free energy calculations, the cubic phase of ceria remains the most stable, while the imaginary mode indicates a change to a thermally disordered cubic phase, with the majority of disorder occurring on the anion sublattice. Our results explain the high temperature ionic conductivity in ceria and other fluorite-structured materials in terms of the intrinsic lattice dynamics, and give insight to the stability and anionic disorder at elevated temperatures.

I. INTRODUCTION

Cerium dioxide (CeO_2, or ceria) is an insulating rare earth metal oxide with a wide band gap and high thermal stability. It is used for a wide range of applications including glass polishing,[1–3] ceramics,[4,5] nanomedicine,[6,7] solid state electrochemistry,[8–10] and as a high-κ dielectric replacement for SiO_2 in metal-oxide-semiconductor field effect transistors (MOSFETs).[11–15] It is also of technological interest to the field of catalysis, where it can be used as a catalyst itself[16–18] or as a support material.[19–21] The basis of this application is the low energy of formation of oxygen vacancies, which allows the material to absorb oxygen under oxidizing conditions and release oxygen under reducing conditions.

Ceria stabilizes in the cubic fluorite phase (space group $Fm\bar{3}m$) at ambient conditions and remains stable in this phase over a remarkably wide range of temperature,[22,23] doping concentration,[8,24,25] and level of nonstoichiometry.[22,23] Coupled with this large stability range is a high ionic conductivity, related to the low energy of formation of oxygen vacancies.[8,26,27] How the material remains stable at high temperatures, however, with a large degree of disorder in the anion sublattice, is not well understood.

The observed high ionic conductivity opens the possibility of using ceria as a solid electrolyte in solid oxide fuel cells (SOFCs)[8–10] operating in the medium temperature range (600–900 K), where problems associated with start-up times and sealing are reduced.[28] In this temperature range, ionic conduction is mediated by the presence of oxygen vacancies, which form both under the reducing conditions present in the cell and due to the presence of impurities. In order to avoid short circuiting the fuel cell, an ideal electrolyte will have high ionic and negligibly low electronic conductivity. In ceria, however, the formation of small polarons associated with oxygen vacancy formation (i.e., the reduction of Ce^{IV} to Ce^{III} to maintain charge neutrality) leads to electronic conduction in the material.[26,29–31] The presence of the effectively larger Ce^{III} cation also introduces a strain, which leads to an expansion of the lattice in a process known as "chemical expansion."[8,24,32–36] This strain can produce macroscopic effects such as cracks which severely restrict the operational capability of the fuel cell. To minimize these undesirable effects in SOFC applications, doping with trivalent impurities such as Gd[37] and Sm[38] has been proposed; these dopants are charge compensated by the formation of oxygen vacancies, without the associated reduction of Ce^{IV}, and, as their ionic radii are close to that of the host Ce^{IV} cation, their presence leads to a reduced chemical expansion. Increasing the doping concentration increases the oxygen vacancy concentration, and initially increases the ionic conductivity. At doping concentrations above ∼20%, however, the conductivity reduces dramatically as defect complexes form. These act as deep traps for the oxygen vacancies, thus restricting the mobility of anions.

An interesting observation was made by Hohnke[39] when measuring the ionic conductivity of Gd-doped ceria samples over a wide range of temperature. At low and medium temperatures, conductivity increased with temperature at a higher rate for samples with higher Gd concentrations, which is as one would expect; the oxygen vacancy concentration depends on the concentration of Gd impurities, and greater oxygen vacancy concentrations will mean a greater anionic conductivity as temperature is increased. At temperatures above ∼1600 K, however, the same conductivity was approached regardless of the doping concentration in the sample. The trend in ionic

conductivity versus temperature for the different samples also converged above this temperature. The author attributed this to a possible saturation in the concentration of oxygen vacancies in the samples. The level of nonstoichiometry of pure ceria (x in CeO_{2-x}) at this temperature in air is $x \approx 0.001$,[40] which is at least an order of magnitude lower than that which would be present due to the Gd doping (up to 20% in the work of Hohnke). The reduction of ceria, therefore, is unlikely to lead to the concentrations of vacancies required to account for the convergence in conductivity versus temperature trends observed by Hohnke; it is possible that these results indicate a change in the mechanism of ionic conduction at elevated temperatures, from one purely mediated by oxygen vacancies.

The structural disorder of ceria at elevated temperatures (up to 1770 K) was studied experimentally by Yashima *et al.*[41] They used neutron diffraction followed by a combination of Rietveld analysis, the maximum-entropy method (MEM), and MEM-based pattern fitting to determine the nuclear density distribution of ceria at various temperatures. The cubic fluorite structure can be pictured as consisting of a face-centered-cubic (fcc) lattice of cations, with all tetrahedral holes occupied by anions, so that the anions form a simple cubic sublattice. The octahedral hole in the fcc cation sublattice provides an interstitial site for the anions. The analysis of Yashima *et al.* demonstrated that oxygen in ceria has a complicated disorder, spreading over a much wider region than that of cerium. They found evidence for anistropic thermal motions of oxygen about their ideal site, with increased motions along the [111] direction towards the interstitial site, which increased with increasing temperature. This suggests a diffusion mechanism mediated by anion Frenkel pairs, which form when oxygens move from their ideal lattice site to the interstitial site. This mechanism becomes more favorable when the lattice is thermally expanded. Their data were also consistent with a slightly curved diffusion path along the [001] direction, where anions traverse the octahedron surrounding the interstitial site while not occupying the site itself.

At temperatures close to, but below, their melting points cubic fluorite structured materials are known to undergo a transition to the "superionic" regime, characterized by a dramatic increase in ionic conductivity[42–44] while electronic conductivity remains low. This transition is associated with a large dynamic disorder of the anion sublattice, where transport of anions occurs via a hopping mechanism,[42,45–48] though the details are still not completely understood.[44] This mechanism of conduction may play a role in ceria at elevated temperatures; superionic conductivity has been observed in ultrathin Gd-doped ceria[49] and Sm-doped ceria nanocomposites[50] at relatively low temperatures (under 900 K), but in these cases was attributed to grain-boundary and size effects.

In this paper we study the static and dynamic stability of ceria over a range of values of isotropic strain, ε, defined as

$$\varepsilon = \frac{a - a_0}{a_0} \qquad (1)$$

(where a_0 is the equilibrium lattice constant and a is the strained lattice constant). We use density functional theory (DFT) in the generalized gradient approximation to exchange and correlation, with a Hubbard U parameter applied to f electrons of Ce (GGA $+ U$), to calculate the force constants and

derive the elastic constants and dynamical matrix. Calculations are further validated for certain values of strain and reciprocal lattice vector using a hybrid density functional, which provides a more accurate and unbiased description of the electronic structure, but is substantionally more computationally intense than standard DFT. We find good agreement between the two approaches. At the X point in the reciprocal lattice, the B_{1u} mode, consisting of oxygen motions in the [001] direction, softens considerably as the lattice is expanded. At $\varepsilon = 0.016$, the B_{1u} mode crosses the E_u doublet (which involves oxygen motion perpendicular to [001]). A maximum in the density of phonon states occurs at the crossing point. We propose that the modes couple, resulting in an increased probability of anion interstitial site occupation. We infer that this leads to a transition to an ionic conductivity regime dominated by a mechanism mediated by anions occupying, or moving close to, the interstitial site. Given the experimentally determined relationhip between temperature and lattice expansion in ceria,[41,51] a strain of 1.6% corresponds to a temperature $T = 1600$ K, which is the value of T at which Hohnke[39] observed the convergence in ionic conductivity for samples with different Gd concentrations. As the lattice is expanded further, the B_{1u} mode continues to soften, becoming imaginary at $\varepsilon = 0.034$, which corresponds to $T = 2500$ K (close to, but below, the melting point of ~ 2800 K[8]). Following the imaginary mode results in a transition from the cubic to a tetragonal phase, similar to what is observed in zirconia[52] and hafnia.[53] From our calculated values of the elastic constants, however, we find that the structure remains mechanically stable at this level of expansion. Using a shell interatomic potential model, which describes the lattice dynamics of the expanded cell in reasonable agreement with our DFT approach, we calculate the free energies of the two phases in the quasiharmonic approximation, finding the cubic phase to remain the more stable as the mode becomes imaginary. We therefore attribute the appearance of the imaginary mode to a change to a thermally disordered phase, where the material remains on average cubic, with the majority of the thermal disorder occurring in the anion sublattice.

The rest of the paper is as follows: in Sec. II details of our calculations are given, in Sec. III we present and discuss our results, and in Sec. IV we summarize the main findings of our study.

II. CALCULATIONS

We have used DFT to calculate the equilibrium structure of bulk ceria and the force constants at a range of positive and negative isotropic linear strains. All our DFT calculations were carried out using the VASP code,[54–57] utilizing the solids-corrected Perdew-Burke-Ernzerhof (PBEsol) GGA exchange-correlation (XC) functional[58,59] with the projector augmented wave (PAW) method.[60] To correct the self-interaction error present in DFT, we have taken two approaches. The first was to apply a Hubbard U parameter ($U = 5$ eV) on the Ce_{4f} (GGA $+ U$), which has been shown to give accurate descriptions of the localized nature of n-type defects in ceria.[15,35,61–65] The second was to use hybrid exchange correlation functionals (hybrid-DFT), where a percentage of exact exchange is included. For this we used the screened

TABLE I. Calculated structural, elastic, and dielectric properties of CeO_2 at ambient pressure compared with previous experimental and theoretical results in the literature.

	This work		Previous work in the literature				
	GGA + U	HSE06	GGA + U[61]	LDA + U[75]	LDA[76]	LDA[77]	Experiment
a_0 (Å)	5.431	5.399	5.470	5.400	5.366	5.37	5.401,[78] 5.407,[41] 5.408,[22] 5.411[32]
B_0 (GPa)	200.0	207.5	172	211.1	210.1	203.6	200,[79] 220,[80] 230,[81] 236[82]
B_0'	4.4	4.4		4.4	4.4	4.4	4,[79] 4,[81] 4.4,[80] 4.4[82]
C_{11} (GPa)	371.83			354.790	386	371.40	403[83]
C_{12} (GPa)	114.69			139.272	124	117.89	105[83]
C_{44} (GPa)	62.71			51.195	73	68.10	60[83]
ϵ^∞	6.546			6.791	6.23		5.31,[84] 6[85]
Z^* Ce	5.525			5.479	5.712		
Z^* O	−2.764			−2.740	−2.856		

HSE06[66] functional. Although hybrid functionals provide a more accurate description of electronic structure, they are approximately an order of magnitude more computationally intense than local density approximation (LDA) and GGA functionals, so we limited their application in this study to certain reciprocal lattice vectors and values of strain. Full phonon dispersions were determined using the GGA + U approach.

To avoid the problem of Pulay stress, the energy and gradient of the three atom primitive unit cell of CeO_2 was calculated at a series of different volumes with an 800 eV plane wave cutoff and an $8 \times 8 \times 8$ Monkhorst-Pack[67] k-point mesh, which provided convergence in the total energy up to 10^{-5} eV. The resulting energy-volume data was fitted to the Murnaghan equation of state to derive the equilibrium lattice constant and bulk modulus.

Phonon frequencies of CeO_2 were determined using the frozen phonon approach, where the dynamical matrix is derived by displacing atoms from their equilibrium positions and calculating the resulting forces, thus giving the force constants. All force calculations were deemed converged when the change in total force on each ion per self-consistent field iteration was less than 10^{-4} eV Å^{-1}. Phonon dispersions of CeO_2 at different values of lattice constant were calculated (using GGA + U) by making appropriate atomic displacements in a $4 \times 4 \times 4$ (192 atoms) expansion of the primitive unit cell and constructing the dynamical matrix, as implemented in the postprocessing program PHONOPY.[68] The splitting between the transverse optical (TO) and longitudinal optical (LO) modes was determined using a nonanalytical correction term,[69–71] which required knowledge of the high frequency dielectric constant and Born effective charges. We have used linear response in our GGA + U approach to determine these properties at the different values of strain studied, as implemented in VASP. Using our hybrid functional approach we have determined phonon frequencies at the Γ, L, and X points in the reciprocal lattice using a $2 \times 2 \times 2$ expansion (24 atoms) of the unit cell, and at the Γ and X points only using the cubic unit cell (12 atoms). The elastic constants were determined from the stress-strain relation by performing six finite distortions of the lattice, using our GGA + U approach, as implemented in VASP.

We have used a modified version of the shell-polarizable interatomic potential model developed previously,[72,73] which

gives accurate results on lattice dynamics at zero strain while maintaining good qualitative agreement with our DFT approaches at large strains, to calculate the vibrational contribution to the free energy of the relevant phases of CeO_2, under the quasiharmonic approximation. Our aim here is to test the stability of the phases at temperatures above 2000 K at a significantly reduced computational cost. We have used GULP[74] to perform these calculations.

III. RESULTS

A. Equilibrium properties of ceria

In Table I we present our calculated values of lattice constant (a_0), bulk modulus (B_0) and its pressure derivative (B_0'), elastic constants (C_{11}, C_{12}, and C_{44}), high-frequency dielectric constant (ϵ^∞), and Born effective charges (Z^*) of CeO_2 in the cubic fluorite phase, compared with previous experimental and theoretical results from the literature. We find excellent agreement between our calculated a_0 and the low temperature experimental value of Gupta et al.,[78] with our GGA + U approach differing by 0.5% and our HSE06 hybrid-DFT approach differing by less than 0.05%. In the GGA + U approach, using the PBEsol functional gives an improvement of 0.7% in a_0, when compared to experiment, over using the PBE functional.[61–65] Our values of B_0 and B_0' also agree well with experiment.[80,81,83] We have calculated the elastic constants, ϵ^∞ and Z^* using GGA + U. We find good agreement with experiment[83] in our values of C_{11}, C_{12}, and C_{44}, with the largest discrepancy (7.7%) occurring for C_{11}. This latter discrepancy could be attributed to an overestimation of the lattice constant by our GGA + U approach. Our results agree well with the calculations of Shi et al.[75] at the LDA + U level of theory and are in excellent agreement with previous calculations at the LDA level.[76,77] Our calculated value of ϵ^∞ is higher than experiment[84,85] but agrees well with previous calculations at a similar level of theory,[75,76,86] as do our calculated Born effective charges.

B. Dynamical properties of ceria

Our calculated phonon dispersion using GGA + U is shown in Fig. 1, compared with the Raman scattering measurements of Nakajima et al.[83] and Kouroklis et al.,[87] the infrared
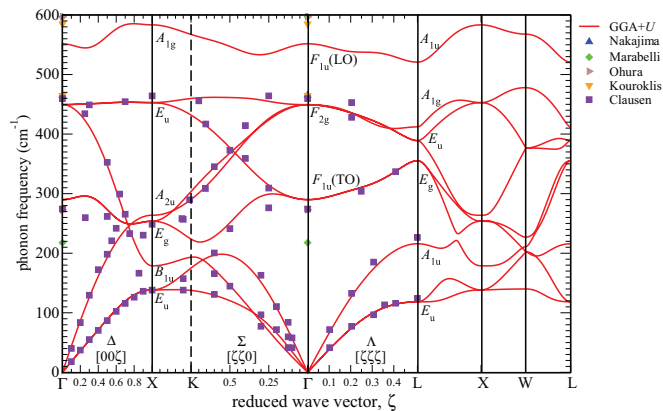
FIG. 1. (Color online) Phonon dispersion curve for CeO_2 calculated using $GGA+U$ (solid red line) compared with measurements using Raman scattering (blue upward-pointing and orange downward-pointing triangles; Refs. [87] and [83]), infrared spectroscopy (sidewards-pointing brown triangles; Ref. [88]), reflectivity-derived (green diamonds; Ref. [89]), and inelastic neutron scattering (purple squares; Ref. [90]) methods. The modes are labeled according to their symmetry representations at the Γ, X, and L points.

spectroscopy measurements of Ohura,[88] the results of Marabelli *et al.* derived from reflectivity measurements,[89] and the inelastic neutron scattering measurements of Clausen *et al.*[90] These experimental measurements were carried out at room temperature (RT); in principle, a more accurate comparison between the data sets may be achieved by performing the $GGA+U$ dispersion calculation with the lattice expanded by an amount corresponding to the thermal expansion at RT. The experimentally determined thermal expansion coefficient at RT, however, is $\sim (10\text{–}11) \times 10^{-6} \text{ K}^{-1}$.[78,91] The change in the calculated frequencies when the lattice is expanded by an amount corresponding to this thermal expansion is within the overall error in the results. For this reason we have chosen to perform the calculations at the athermal limit.

A comparison of the phonon frequencies in Fig. 1 shows that our $GGA+U$ approach agrees well with experiment, in particular in reproducing the acoustic mode dispersion. Our calculated acoustic mode frequencies agree with the measurements of Clausen *et al.*[90] within $\sim 1\%$, apart from the longitudinal acoustic (LA) mode at the L point, which we find is 4% lower than the value they report. We find less good agreement, however, between our calculated infrared-active F_{1u} LO-TO mode splitting and experiment. We calculate the F_{1u} LO phonon mode at Γ (ω_{LO}) to be $\omega_{LO} = 552 \text{ cm}^{-1}$, which is $\sim 7.5\%$ lower than the experimental results of Marabelli *et al.*[89] and Ohura.[88] We note that our calculation of the LO-TO mode splitting is determined using a nonanalytical correction term,[69–71] which depends on ϵ^∞ and the Born effective charges Z^*. We have used our calculated values for ϵ^∞ and Z^* (see Table I) when determining the splitting. If instead we use the experimental value of $\epsilon^\infty = 5.31$,[84] we find that $\omega_{LO} = 596 \text{ cm}^{-1}$, which is within 0.2% of experiment.[87,88] Our calculated dispersion is in excellent agreement with previous calculations at a DFT-LDA level of theory.[75,76] One detail evident from our results but not observed in the calculations of

Gürel *et al.*[76] and Shi *et al.*[75] is the crossing of the longitudinal and transverse branches of the Raman active (F_{2g} at the Γ point) mode at $\sim 420 \text{ cm}^{-1}$ in the $\Gamma \to L$ direction ($[\zeta\zeta\zeta]$ in Fig. 1). Along this direction the triply degenerate (at the Γ point) F_{2g} mode splits into a doublet and singlet (transverse and longitudinal, respectively). This branch crossing, which was not reproduced by Clausen *et al.*[90] in their shell model, explains their labeling of the modes along these branches. They predicted a singlet mode frequency lower than that of the doublet at the L point. From our results we see that the longitudinal branch does fall below the transverse branch at the point (0.2,0.2,0.2) along the $[\zeta\zeta\zeta]$ direction (measured in units of $2\pi/a_0$), but the branches cross once more at the point (0.4,0.4,0.4), resulting in a higher singlet mode frequency than the doublet at the L point, as would be expected.

C. Dynamical properties as a function of isotropic strain

Our results for the effect of applying positive and negative ε to the lattice, i.e., expansion and contraction, on the calculated phonon dispersion using $GGA+U$ are shown in Fig. 2, along
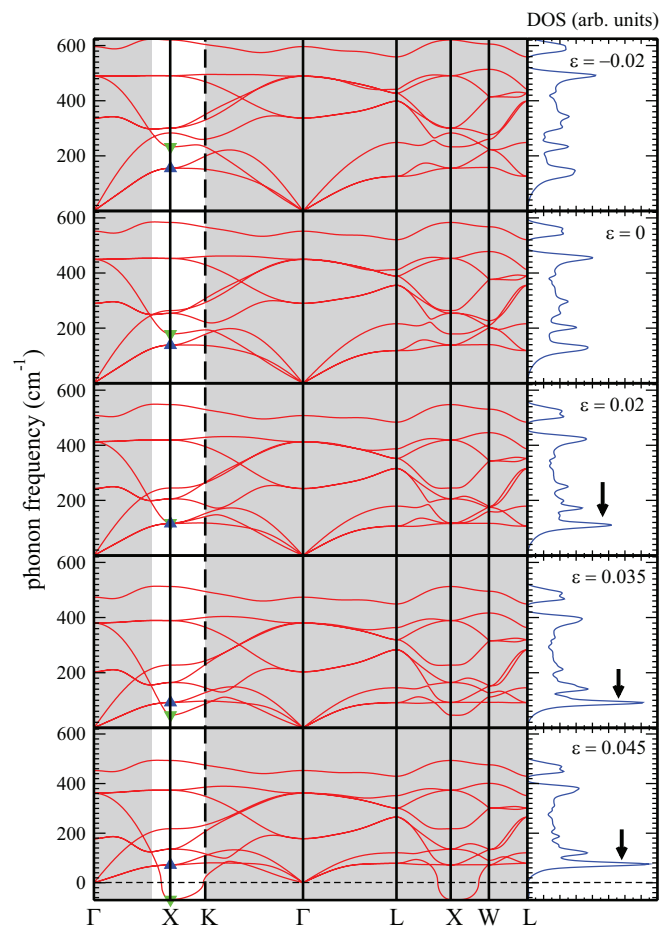

FIG. 2. (Color online) Phonon dispersion curves and densities of states for CeO_2 determined using $GGA+U$ at different values of linear strain ε. The horizontal axis is labeled according to the convention of Fig. 1. At the X point, the B_{1u} singlet is indicated by the downward-pointing (green) triangle, while the E_u doublet is indicated by the upwards-pointing (blue) triangle. The unshaded region highlights the softening of the B_{1u} mode at the X point.

with the calculated phonon density of states (PDOS). Changing the value of ε is equivalent to applying a pressure p to the lattice. From our GGA + U approach we can determine this pressure. We found that p as a function of ε was fitted well (with a χ-squared value under 10^{-3}) by the following polynomial:

$$p = 3806\varepsilon^2 - 607.7\varepsilon (\text{GPa}), \qquad (2)$$

e.g., a strain of $\varepsilon = -0.02$ gives a pressure $p = 13.7$ GPa.

We first consider the case of negative ε (contraction). Negative ε results in a stiffening of the lattice and a corresponding increase in phonon frequencies. The F_{2g} mode determined at 449 cm^{-1} shifts to 489 cm^{-1} at $\varepsilon = -0.02$, i.e., at $p = 13.7$ GPa. Kouroklis *et al.*[87] measured this mode to be 464 cm^{-1} at ambient pressure, increasing to 507 cm^{-1} at $p = 13.4$ GPa. Xiao *et al.*,[79] using Raman measurements, found that this mode increased to 501 cm^{-1} at $p = 12.0$ GPa. Our results are in good agreement with these experimental results.

We now turn to the case of positive ε (expansion). From Fig. 2 we note that increasing ε leads to an overall softening of the phonon modes, as the material itself becomes softer. The effect is small, apart from the B_{1u} singlet mode at the X point, which softens considerably as the lattice is expanded (see the unshaded region in Fig. 2). This mode crosses the E_u doublet at the X point when $\varepsilon = 0.02$, and becomes imaginary (indicated by negative frequency) when $0.035 < \varepsilon < 0.045$. A maximum peak in the PDOS (indicated by an arrow in Fig. 2) is observed, at the frequency at which the B_{1u} and E_u modes intersect at (or close to) the X point, and increases in magnitude as the strain is increased. We note that this crossing coincides with an overall flattening of the lower acoustic band away from the Γ point. The crossing of the B_{1u} and E_u modes at the X point is shown more clearly in Fig. 3, where we have plotted their frequencies
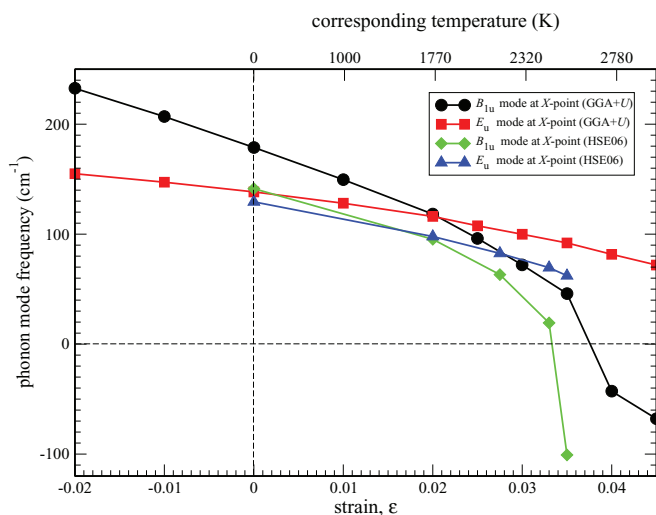
as a function of ε. We have also determined a temperature scale that corresponds to the level of strain studied, which we have shown in Fig. 3, for which we have combined the data of Sameshima *et al.*[51] (valid for the temperature range 298–1473 K), and the data of Yashima *et al.*[41] (valid for temperatures up to 1770 K). The two experimental data sets are in good agreement in the temperature range common to both. For temperatures above 1770 K, we have applied a quadratic fit to the data of Yashima *et al.* (with a χ-squared value of $\sim 10^{-3}$).

D. B_{1u} mode softening at the X point

To study the effect of strain on the B_{1u} mode in particular, we have performed hybrid-DFT calculations of the phonon modes. Hybrid functionals (such as HSE06) provide a marked improvement in description of the electronic structure,[66,92–94] resulting in more accurate structural properties (see Table I) and descriptions of the potential energy landscape. We therefore expect hybrid DFT to provide an improved description of the phonon dispersion in comparison with GGA + U. As hybrid DFT is significantly more computationally intense in comparison to GGA + U, we limit our application of this approach. We have performed force constant calculations using a $2 \times 2 \times 2$ expansion of the primitive unit cell for $\varepsilon = 0$ and $\varepsilon = 0.035$. This supercell size provides phonon frequencies at the Γ, X, and L points. We present our results for all calculated frequencies at these reciprocal lattice points in Table II, shown in comparison to our GGA + U calculated values and experimental results,[83,87–90] where available. For our hybrid-DFT calculations we have used the experimental value of $\epsilon^{\infty} = 5.31$[84] when determining the nonanalytical correction term to account for F_{1u} TO-LO splitting at Γ. Hybrid DFT gives us an improved description of the optical modes at the Γ point, and the high frequency E_u mode at the X point, but no significant improvement over GGA + U for the low frequency acoustic modes at the X and L points. To study the softening of the B_{1u} mode at the X point using hybrid DFT, we performed further calculations of the force constants using a cubic (12 atom) cell (this cell provides phonon frequencies at the Γ and X points only). We plot our results for the B_{1u} and E_u modes at the X point as a function of ε and T in Fig. 3.

Using our hybrid-DFT (GGA + U) approach, we find that the two modes cross at $\varepsilon = 0.016$ ($\varepsilon = 0.02$), corresponding to $T = 1600$ K ($T = 1770$ K), and that the B_{1u} mode becomes imaginary at $\varepsilon = 0.034$ ($\varepsilon = 0.038$), corresponding to $T = 2500$ K ($T = 2700$ K). Schematics of the two modes (singlet and doublet) are shown in Fig. 4. The B_{1u} mode is a singlet [Fig. 4(a)], consisting of motions of the O ions in the [001] direction, with no motion of the Ce ions. If we consider the O sublattice to contain chains of oxygen ions in the [001] direction, we observe that, along the chains, the oxygens move in phase, with adjacent chains moving opposite in phase. The E_u mode is a doublet [Figs. 4(b) and 4(c)], consisting of both Ce and O motion. All motion occurs perpendicular to the [001] direction. Alternating layers of Ce along the [001] direction move in opposite phases. The O motion is at right angles to that of Ce. Adjacent O ions move in opposite phases, so that the motion consists of a series of alternating oxygen-oxygen stretch modes. In this mode, the amplitude of motion of the

FIG. 3. (Color online) Calculated B_{1u} and E_u mode frequencies at the X point as a function of linear strain ε, determined using GGA + U (black circles and red squares, respectively), and hybrid-DFT with the HSE06 functional (green diamonds and blue triangles, respectively). The lines are a guide for the eye. Negative frequency indicates an imaginary mode.

TABLE II. Calculated phonon mode frequencies of CeO$_2$ at the high symmetry points of the Brillouin zone Γ, X, and L determined using GGA + U and hybrid DFT using the HSE06 functional, shown in comparison to experimental results where available. The results are shown for different values of strain, ε. Negative frequency indicates an imaginary mode (unit: cm^{-1}).

			$\varepsilon = 0$								
	Γ				X				L		
Mode	GGA+U	HSE06	Expt.	Mode	GGA+U	HSE06	Expt.	Mode	GGA+U	HSE06	Expt.
F_{1u} (LO)	552	591	585,[87] 597[88,89]	A_{1g}	583	611		A_{1u}	521	543	
F_{2g}	449	451	460,[90] 465[83,87]	E_u	453	460	464[90]	A_{1g}	412	427	
F_{1u} (TO)	290	269	218,[89] 273,[88] 274,[90] 275[87]	A_{2u}	264	275		E_u	389	384	
				E_g	254	224	249[90]	E_g	355	348	
				B_{1u}	179	141		A_{1u}	216	207	227[90]
				E_u	138	129	138[90]	E_u	118	116	124[90]
			$\varepsilon = 0.035$								
	Γ				X				L		
Mode	GGA+U	HSE06	Expt.	Mode	GGA+U	HSE06	Expt.	Mode	GGA+U	HSE06	Expt.
F_{1u} (LO)	474	529		A_{1g}	513	540		A_{1u}	449	472	
F_{2g}	380	382		E_u	389	400		A_{1g}	364	382	
F_{1u} (TO)	203	175		A_{2u}	228	240		E_u	320	314	
				E_g	164	116		E_g	283	278	
				E_u	92	62		A_{1u}	145	124	
				B_{1u}	46	−101		E_u	91	73	

Ce ions is a factor of ~10 times that of O at $\varepsilon = 0$, but this factor reduces as the cell is expanded, so that at $\varepsilon = 0.04$ the Ce amplitude is three times the amplitude of O.

E. Coupling of the B_{1u} and E_u modes

When the B_{1u} and E_u modes cross at the X point, there is an associated large, narrow peak in the PDOS (indicated by an arrow in Fig. 2). This implies that the occupation of these modes will be high at large temperatures. If there is a large amount of (in-phase) atomic motion consisting of these modes, with relatively large amplitudes at higher temperatures, there will be an increased probability of a coupling, or combination, of the modes. We illustrate the resulting motion when the B_{1u} and E_u modes combine at the X point in Fig. 5. For clarity we only show the motion of a single oxygen chain in the [001] direction, with the adjacent chains not shown. We also show the relevant Ce motion in the vicinity of the oxygen chain. The interstitial site is in the center of the cube formed by the Ce

ions (indicated by a black cross). When the modes combine, there is an alternating effect along the [001] oxygen chain. One oxygen ion (O1 in Fig. 5) moves towards the interstitial site, with a Ce (Ce1 in Fig. 5) moving closer to this site, providing a possible further stabilization for the oxygen. The next oxygen ion (O2 in Fig. 5) along [001] moves towards a Ce site, with the Ce ion (Ce2 in Fig. 5) moving away from this site. There is an equivalent Ce ion (Ce3 in Fig. 5) moving towards the Ce site along [1$\bar{1}$0], which, as the Ce motion is greater than the oxygen motion perpendicular to [001], may lead to a "straightening" of the motion of this O ion in [001] direction. The pattern is repeated on moving along the [001] direction. The pattern is also repeated for different chains of oxygen ions along [001], but for each chain, a different interstitial site is involved in the motion.

1. Implications for ionic conductivity

The overall effect of this combined motion will be an increased probability of occupation of the interstitial site by
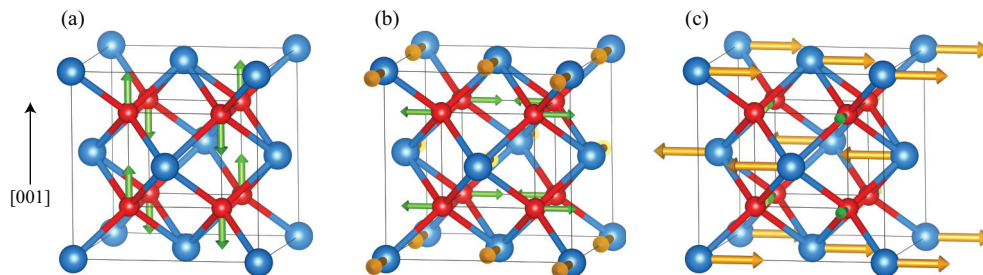

FIG. 4. (Color online) Schematic of the eigenvectors associated with (a) the B_{1u} singlet mode and (b),(c) the E_u doublet mode at the X point. O (dark-gray/red spheres) atomic motion is indicated by dark-gray (green) arrows. Ce (light-gray/blue spheres) atomic motion is indicated by light-gray (orange) arrows. The eigenvectors are shown in the cubic unit cell with the simple cubic anion sublattice highlighted. The lengths of the arrows indicate the relative proportion of the magnitude of the O and Ce atomic motions, which reduces as the lattice is expanded (see text).
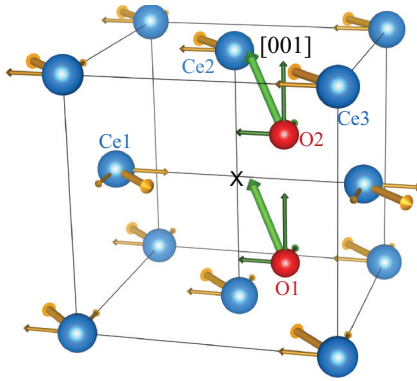
FIG. 5. (Color online) Combination of the B_{1u} and E_u modes at the X point, shown for clarity acting on a single O chain (dark-gray/red spheres) in the [001] direction (adjacent O chains not shown). The interstitial site is represented by a black cross in the center of the cube formed by the Ce ions (light-gray/blue spheres). The motions associated with the B_{1u} and E_u modes are indicated by thinner, darker-colored/shaded arrows, while the resulting motion from the combination of the modes is indicated by thicker, lighter-colored/shaded arrows.

an oxygen ion. From our calculated eigenvectors, we estimate that the amplitude of O motion in the B_{1u} mode is ∼0.5 Å at $T = 1600$ K. In the harmonic approximation, the amplitude of vibration is inversely proportional to the square root of the frequency. As ε is increased, the mode frequency reduces, leading to an increase in the amplitude.[115] The motion of the oxygens in the [001] direction is greater than their motion perpendicular to it, but as ε is increased, the oxygen motion perpendicular to [001] increases. This, combined with the overall increase in amplitude as the frequency reduces, will lead to an increase in the probability of the anion approaching the interstitial site, facilitating ionic transport in the [001] direction in a caterpillarlike mechanism, where each oxygen ion moves to the site vacated by its nearest-neighbor (as a result of an oxygen occupying the interstitial site), i.e., the conductivity is mediated by Frenkel-like disorder. When the B_{1u} and E_u modes combine, there will be a switch to this mechanism of ionic conduction, which will be independent of the number of oxygen vacancies present due to reduction or the presence of impurities. Since we predict the mode coupling to occur at $\varepsilon = 0.016$, or $T = 1600$ K, this provides an explanation for the observations of Hohnke.[39] As the temperature rises above 1600 K, the predominant ionic conductivity mechanism switches from that mediated by the oxygen vacancies present in the samples due to the Gd impurities and/or reduction to that mediated by the anion interstitial site occupation resulting from the coupling of the B_{1u} and E_u modes at the X point. There is therefore a convergence in ionic conductivity for the samples containing different Gd concentrations, and also a convergence in the rate of increase in ionic conductivity as the temperature is increased further. Our results are also consistent with the observation of Yashima *et al.*[41] Their nuclear density distribution measurements indicated increased motion of oxygen in the [111] direction (i.e., towards the interstitial site), which suggested a curved diffusion path along [001], similar to the diffusion mechanism we are proposing

(we note that Yashima *et al.* concluded that their data was also consistent with a diffusion path along the [111] direction).

Similar mechanisms of ionic conductivity in fluorite-structured materials have been proposed previously for UO_2,[42,95,96] PbF_2,[97,98] CaF_2, BaF_2, and SrF_2.[43,99] When studying the effect of expansion on the antifluorite Li_2O, Gupta *et al.*[100] and Fracchia *et al.*[101] observed a similar softening of the B_{1u} mode at the X point as we have calculated for ceria. In the case of Li_2O, however, the B_{1u} mode is the lowest in frequency at the X point at equilibrium. As the lattice is expanded, the B_{1u} mode softens and becomes imaginary at $T = 1200$ K, close to, but below, the melting point. In both studies the authors attributed the imaginary mode to a change to a superionic conductivity regime, mediated by cation hopping (as Li_2O is an antifluorite) along [001]. This conclusion does not necessarily follow, however, as the imaginary mode may indicate either a structural phase change or a change to a thermally disordered phase (see below). A more convincing argument was made by Garvartin *et al.*,[102] who calculated a crossing of the transverse Raman and LO modes at temperatures above 1000 K in Li_2O. They attributed this to a change to a conductivity regime mediated by a caterpillarlike mechanism, similar to what we propose for ceria. They further validated their results using molecular dynamics (MD) simulations. Guglielmetti *et al.*[103] have performed an MD study on defect formation and stability in ceria using empirical potentials. They found that anion Frenkel recombination became more favorable at higher temperatures, and that, for anions, interstitial migration was faster than vacancy migration at temperatures above 1700 K. Their results are consistent with our proposed conductivity mechanism at elevated temperatures. Our work, however, demonstrates the basis of the effect in the temperature dependent lattice dynamics of the material. Further calculations of defect formation and migration, which will complement our present study, are underway and will be reported elsewhere.

2. Implications for nanoclusters

Tsunekawa *et al.*[104,105] and Wu *et al.*[106] reported that below a certain size, ceria experiences an anomalous lattice expansion, where average bond length within particles increases significantly. This phenomenon has been rationalized as an effect of reduction, with ceria nanoparticles rapidly losing oxygen as the surface area to volume ratio of the particle increases. Concomitantly, Weber *et al.*[107] observed a broadening of the Raman peak as the ceria particle size decreased. Our findings provide a direct link between the two effects: Expansion of the lattice as the particle size decreases will lead to a coupling of modes, providing favorable conditions for phonon-phonon scattering, which will result in the observed broadening. Moreover, this expansion also provides grounds for the low-temperature disorder or phase transitions reported to occur in ceria at the nanoscale.[108–110]

F. Stability of ceria at elevated temperatures

From our hybrid-DFT (GGA + U) calculations, we determine that the B_{1u} mode becomes imaginary at the X point at $\varepsilon = 0.034$ ($\varepsilon = 0.038$), corresponding to $T = 2500$ K
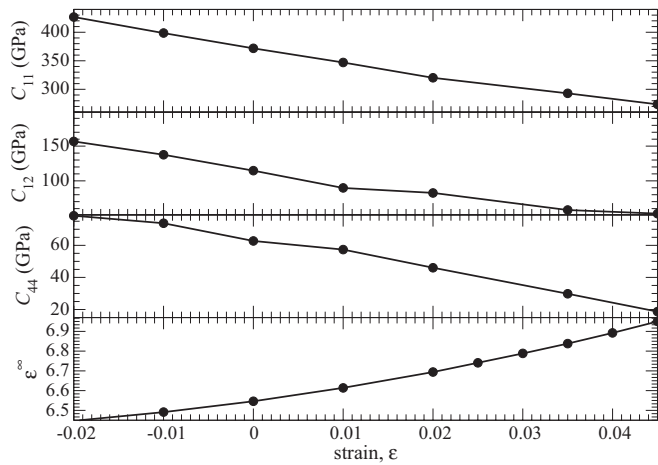
FIG. 6. Calculated elastic constants C_{11}, C_{12}, C_{44}, and high frequency dielectric constant ϵ^{∞}, as a function of linear strain ε, determined using GGA + U (black circles). The lines are a guide for the eye.

($T = 2700$ K). These temperatures are close to, but below, the melting point ($\sim$2800 K[8]) of ceria. Moving beyond the harmonic approximation, we made appropriate displacements along this mode and relaxed the structure (using GGA + U), determining that this imaginary mode corresponds to a phase change to a tetragonal structure.[116] A similar phase change is observed in zirconia[52] and hafnia.[53] Experimental data on the phase diagram of ceria,[22,23] however, indicates that the cubic structure is the only stable phase at elevated temperatures (although we have found no data in the literature for temperatures above 1773 K). We note that, in contrast, at the nanoscale, a hypothetical symmetry-broken phase has been observed indirectly via a characteristic tetragonal splitting of the Raman mode.[110] We have calculated the elastic constants (and high frequency dielectric constant) as a function of applied strain using GGA + U (see Fig. 6). Our results show that the phase stability criteria $C_{44} > 0$, $C_{11} - C_{12} > 0$, and $C_{11} + 2C_{12} > 0$ are satisfied at all values of ε studied, including $\varepsilon > 0.038$, where the B_{1u} mode at the X point is imaginary, thus indicating that the cubic phase remains elastically stable, even with the imaginary mode.

To study this phase stability further, we have performed free energy calculations on the cubic and tetragonal phases using a modified shell interatomic potential model.[72] The model we use is in excellent agreement with neutron inelastic scattering data,[90] and reproduces well the results of our DFT calculations on the dynamical behavior of ceria as a function of ε, while being substantially less computationally intense. We find that, when we include the vibrational contributions to the free energy in the quasiharmonic approximation, the cubic phase is 0.01 eV lower in energy than the tetragonal phase, indicating that the cubic phase is the more stable phase, and indicating that the B_{1u} mode becoming imaginary corresponds to a change to a thermally disordered phase. As the mode consists of O motions only, the majority of the thermal disorder will occur on the O sublattice, leading to the system remaining cubic on average. The temperature at which we determine this transition to occur is in good agreement with MD calculations on doped and undoped ceria by Kovalenko *et al.*,[111] who

found that anion sublattice "melting" occurred in the range 2300–2700 K. Such anion disorder at temperatures below the melting point in cubic fluorite structures has been studied extensively using neutron scattering techniques.[42,43,96–98,112] Moreover, the high ionic conductivity has been associated with the thermal disorder in yttrium-doped zirconia, in particular in its cubic form, stabilized by lattice-mismatched induced strain when interfaced with $SrTiO_3$.[113,114]

IV. CONCLUSIONS

In summary, we have studied the static and dynamic stability of ceria by determining the phonon dispersion for a range of isotropic strains using GGA + U and hybrid DFT. Our calculated properties of the equilibrium structure agree well with experiment and previous calculations. Under expansion, we find a substantial softening of the B_{1u} mode at the X point. Using hybrid-DFT (GGA + U), we determine that, at $\varepsilon = 0.016$ ($\varepsilon = 0.02$), corresponding to $T = 1600$ K ($T = 1770$ K), the B_{1u} and E_u modes cross at the X-point. A large maximum in the PDOS occurs at the frequency at which they cross. By studying the atomic motions involved in the two modes, we infer that they couple, resulting in a significant increase in probability of O atoms occupying, or moving close to, an interstitial site. This provides a mechanism for ionic conductivity, where anions move in the [001] direction. Our proposed temperature at which this occurs is in excellent agreement with measurements of ionic conductivity of Gd-doped ceria samples performed at high temperatures, where it was observed that above 1600 K all samples, regardless of Gd content, approached the same conductivity. As the lattice was expanded further, the B_{1u} mode continued to soften. Using hybrid-DFT (GGA + U), we determined that it became imaginary at $\varepsilon = 0.034$ ($\varepsilon = 0.038$), corresponding to $T = 2500$ K ($T = 2700$ K). We found that the imaginary mode corresponded to a cubic to tetragonal phase transition. Our calculated elastic constants, however, indicated that the cubic structure remains mechanically stable at all values of ε studied. Free energy calculations in the quasiharmonic approximation, performed using an interatomic potential model, indicated that the cubic phase remained the most stable configuration when the B_{1u} mode became imaginary. We therefore attribute the imaginary mode to a transition to a thermally disordered phase which remains cubic on average, with the majority of the disorder occurring in the anion sublattice.

*j.buckeridge@ucl.ac.uk

[1] C. Stanek, A. Tan, S. Owens, and R. Grimes, J. Mater. Sci. **43**, 4157 (2008).

[2] Z. Zhang, L. Yu, W. Liu, and Z. Song, Appl. Surf. Sci. **256**, 3856 (2010).

[3] M. Fu *et al.*, Solid State Sci. **11**, 2133 (2009).

[4] G. Grathwohl and T. Liu, J. Am. Ceram. Soc. **74**, 3028 (1991).

[5] M. Stojmenovi *et al.*, Ceram. Int. **39**, 1249 (2013).

[6] C. Mandoli *et al.*, Adv. Funct. Mater. **20**, 1617 (2010).

[7] F. Pagliari *et al.*, ACS Nano **6**, 3767 (2012).

[8] M. Mogensen, N. M. Sammes, and G. A. Tompsett, Solid State Ionics **129**, 63 (2000).

[9] B. C. H. Steele and A. Heinzel, Nature (London) **414**, 345 (2001).

[10] A. J. Jacobson, Chem. Mater. **22**, 660 (2010).

[11] F.-C. Chiu *et al.*, Jpn. J. Appl. Phys. **48**, 04C014 (2009).

[12] Y. Nishikawa, T. Yamaguchi, M. Yoshiki, H. Satake, and N. Fukushima, Appl. Phys. Lett. **81**, 4386 (2002).

[13] C.-H. Chen, I. Y.-K. Chang, J. Y.-M. Lee, and F.-C. Chiu, Appl. Phys. Lett. **92**, 043507 (2008).

[14] W.-H. Kim *et al.*, J. Electrochem. Soc. **158**, G169 (2011).

[15] P. R. L. Keating, D. O. Scanlon, and G. W. Watson, J. Mater. Chem. C **1**, 1093 (2013).

[16] J.-X. Guo *et al.*, Acta Chim. Sinica **V65**(10), 937 (2007).

[17] K. Krishna, A. Bueno-López, M. Makkee, and J. Moulijn, Top. Catal. **42-43**, 221 (2007).

[18] J. Nunan, M. Cohn, and J. Dormer, Catal. Today **14**, 277 (1992).

[19] W. Deng, C. Carpenter, N. Yi, and M. Flytzani-Stephanopoulos, Top. Catal. **44**, 199 (2007).

[20] P. Panagiotopoulou, J. Papavasiliou, G. Avgouropoulos, T. Ioannides, and D. Kondarides, Chem. Eng. J. **134**, 16 (2007).

[21] M. F. Camellone and S. Fabris, J. Am. Chem. Soc. **131**, 10473 (2009).

[22] O. Sørensen, J. Solid State Chem. **18**, 217 (1976).

[23] I. Riess, M. Ricken, and J. Nölting, J. Solid State Chem. **57**, 314 (1985).

[24] S. Wang, E. Oikawa, and T. Hashimoto, J. Electrochem. Soc. **151**, E46 (2004).

[25] S. Bishop, K. Duncan, and E. Wachsman, Acta Mater. **57**, 3596 (2009).

[26] M. Mogensen, T. Lindegaard, U. R. Hansen, and G. Mogensen, J. Electrochem. Soc. **141**, 2122 (1994).

[27] S. Omar, E. D. Wachsman, J. L. Jones, and J. C. Nino, J. Am. Ceram. Soc. **92**, 2674 (2009).

[28] A. B. Stambouli and E. Traversa, Renew. Sust. Energ. Rev. **6**, 433 (2002).

[29] R. Blumenthal and R. Sharma, J. Solid State Chem. **13**, 360 (1975).

[30] M. Panhans and R. Blumenthal, Solid State Ionics **60**, 279 (1993).

[31] H. L. Tuller and A. S. Nowick, J. Electrochem. Soc. **126**, 209 (1979).

[32] T. Hisashige, Y. Yamamura, and T. Tsuji, J. Alloys Compd. **408–412**, 1153 (2006).

[33] S. Hull *et al.*, J. Solid State Chem. **182**, 2815 (2009).

[34] D. Marrocchelli, S. R. Bishop, H. L. Tuller, and B. Yildiz, Adv. Funct. Mater. **22**, 1958 (2012).

[35] D. Marrocchelli, S. R. Bishop, H. L. Tuller, G. W. Watson, and B. Yildiz, Phys. Chem. Chem. Phys. **14**, 12070 (2012).

[36] S. R. Bishop *et al.*, Energy Environ. Sci. **6**, 1142 (2013).

[37] H. Inaba and H. Tagawa, Solid State Ionics **83**, 1 (1996).

[38] T. Inoue, T. Setoguchi, K. Eguchi, and H. Arai, Solid State Ionics **35**, 285 (1989).

[39] D. Hohnke, Solid State Ionics **5**, 531 (1981).

[40] I. Riess, H. Janczikowski, and J. Nölting, J. Appl. Phys. **61**, 4931 (1987).

[41] M. Yashima, S. Kobayashi, and T. Yasui, Solid State Ionics **177**, 211 (2006).

[42] M. T. Hutchings, J. Chem. Soc., Faraday Trans. 2 **83**, 1083 (1987).

[43] M. T. Hutchings *et al.*, J. Phys. C: Solid State **17**, 3903 (1984).

[44] B. Voronin and S. Volkov, J. Phys. Chem. Solids **62**, 1349 (2001).

[45] C. R. A. Catlow, Comments Solid State Phys. **9**, 157 (1980).

[46] A. Chadwick, Solid State Ionics **8**, 209 (1983).

[47] A. R. Allnatt, A. V. Chadwick, and P. W. M. Jacobs, Proc. R. Soc. A **410**, 385 (1987).

[48] B. Voronin, J. Phys. Chem. Solids **56**, 839 (1995).

[49] H. Huang, T. M. Gür, Y. Saito, and F. Prinz, Appl. Phys. Lett. **89**, 143107 (2006).

[50] Q. Liu and B. Zhu, Appl. Phys. Lett. **97**, 183115 (2010).

[51] S. Sameshima, M. Kawaminami, and Y. Hirata, J. Ceram. Soc. Jpn. **110**, 597 (2002).

[52] C. Wang, M. Zinkevitch, and F. Aldinger, Pure Appl. Chem. **79**, 1731 (2007).

[53] M. Yashima *et al.*, J. Phys. Chem. Solids **57**, 289 (1996).

[54] G. Kresse and J. Hafner, Phys. Rev. B **47**, 558 (1993).

[55] G. Kresse and J. Hafner, Phys. Rev. B **49**, 14251 (1994).

[56] G. Kresse and J. Furthmller, Comput. Mater. Sci. **6**, 15 (1996).

[57] G. Kresse and J. Furthmüller, Phys. Rev. B **54**, 11169 (1996).

[58] J. P. Perdew, K. Burke, and M. Ernzerhof, Phys. Rev. Lett. **77**, 3865 (1996).

[59] J. P. Perdew, A. Ruzsinszky, G. I. Csonka, O. A. Vydrov, G. E. Scuseria, L. A. Constantin, X. Zhou, and K. Burke, Phys. Rev. Lett. **100**, 136406 (2008).

[60] P. E. Blöchl, Phys. Rev. B **50**, 17953 (1994).

[61] M. Nolan, S. Grigoleit, D. C. Sayle, S. C. Parker, and G. W. Watson, Surf. Sci. **576**, 217 (2005).

[62] M. Nolan, J. E. Fearon, and G. W. Watson, Solid State Ionics **177**, 3069 (2006).

[63] N. M. Galea, D. O. Scanlon, B. J. Morgan, and G. W. Watson, Mol. Simul. **35**, 577 (2009).

[64] P. R. L. Keating, D. O. Scanlon, and G. W. Watson, J. Phys.: Condens. Matter **21**, 405502 (2009).

[65] P. R. L. Keating, D. O. Scanlon, B. J. Morgan, N. M. Galea, and G. W. Watson, J. Phys. Chem. C **116**, 2443 (2012).

[66] J. Heyd, G. E. Scuseria, and M. Ernzerhof, J. Chem. Phys. **124**, 219906 (2006).

[67] H. J. Monkhorst and J. D. Pack, Phys. Rev. B **13**, 5188 (1976).

[68] A. Togo, F. Oba, and I. Tanaka, Phys. Rev. B **78**, 134106 (2008).

[69] R. M. Pick, M. H. Cohen, and R. M. Martin, Phys. Rev. B **1**, 910 (1970).

[70] P. Giannozzi, S. de Gironcoli, P. Pavone, and S. Baroni, Phys. Rev. B **43**, 7231 (1991).

[71] X. Gonze and C. Lee, Phys. Rev. B **55**, 10355 (1997).

[72] A. Walsh, S. M. Woodley, C. R. A. Catlow, and A. A. Sokol, Solid State Ionics **184**, 52 (2011).

[73] http://www.ucl.ac.uk/klmc/Potentials/

[74] J. D. Gale and A. L. Rohl, Mol. Simul. **29**, 291 (2003).

[75] S. Shi *et al.*, J. Power Sources **194**, 830 (2009).

[76] T. Gurel and R. Eryigit, Phys. Rev. B **74**, 014302 (2006).

[77] L.-L. Sun, Y. Cheng, and G.-F. Ji, J. At. Mol. Sci. **1**, 143 (2010).

[78] M. L. Gupta and S. Singh, J. Am. Ceram. Soc. **53**, 663 (1970).

[79] W. Xiao, D. Tan, Y. Li, and J. Liu, J. Phys.: Condens. Matter **19**, 425213 (2007).

[80] L. Gerward *et al.*, J. Alloys Compd. **400**, 56 (2005).

[81] S. J. Duclos, Y. K. Vohra, A. L. Ruoff, A. Jayaraman, and G. P. Espinosa, Phys. Rev. B **38**, 7755 (1988).

[82] L. Gerward and J. S. Olsen, Powder Diffr. **8**, 127 (1993).

[83] A. Nakajima, A. Yoshihara, and M. Ishigame, Phys. Rev. B **50**, 13297 (1994).

[84] S. Mochizuki, Phys. Status Solidi B **114**, 189 (1982).

[85] S. Guo, H. Arwin, S. N. Jacobsen, K. Järrendahl, and U. Helmersson, J. Appl. Phys. **77**, 5369 (1995).

[86] T. Yamamoto, H. Momida, T. Hamada, T. Uda, and T. Ohno, Thin Solid Films **486**, 136 (2005).

[87] G. A. Kourouklis, A. Jayaraman, and G. P. Espinosa, Phys. Rev. B **37**, 4250 (1988).

[88] H. Ohura, Master's thesis, University of Tohoku, 1977.

[89] F. Marabelli and P. Wachter, Phys. Rev. B **36**, 1238 (1987).

[90] K. Clausen *et al.*, J. Chem. Soc., Faraday Trans. 2 **83**, 1109 (1987).

[91] R. Körner, M. Ricken, J. Nölting, and I. Riess, J. Solid State Chem. **78**, 136 (1989).

[92] M. Ernzerhof and G. E. Scuseria, J. Chem. Phys. **110**, 5029 (1999).

[93] C. Adamo and V. Barone, J. Chem. Phys. **110**, 6158 (1999).

[94] J. Heyd, G. E. Scuseria, and M. Ernzerhof, J. Chem. Phys. **118**, 8207 (2003).

[95] C. R. A. Catlow, Proc. R. Soc. Lond. A **353**, 533 (1977).

[96] K. Clausen, W. Hayes, J. E. Macdonald, R. Osborn, and M. T. Hutchings, Phys. Rev. Lett. **52**, 1238 (1984).

[97] M. H. Dickens, W. Hayes, M. T. Hutchings, and W. G. Kleppmann, J. Phys. C: Solid State **12**, 17 (1979).

[98] M. H. Dickens, W. Hayes, M. T. Hutchings, and C. Smith, J. Phys. C: Solid State **15**, 4043 (1982).

[99] C. R. A. Catlow, M. J. Norgett, and T. A. Ross, J. Phys. C: Solid State **10**, 1627 (1977).

[100] M. K. Gupta, P. Goel, R. Mittal, N. Choudhury, and S. L. Chaplot, Phys. Rev. B **85**, 184304 (2012).

[101] R. Fracchia, G. Barrera, N. Allan, T. Barron, and W. Mackrodt, J. Phys. Chem. Solids **59**, 435 (1998).

[102] J. L. Gavartin, C. R. A. Catlow, A. L. Shluger, P. W. M. Jacobs, and Z. A. Rycerz, Radiat. Eff. Defects Solids **134**, 107 (1995).

[103] A. Guglielmetti *et al.*, Nucl. Instrum. Meth. B **266**, 5120 (2008).

[104] S. Tsunekawa, R. Sivamohan, S. Ito, A. Kasuya, and T. Fukuda, Nanostruct. Mater. **11**, 141 (1999).

[105] S. Tsunekawa, K. Ishikawa, Z.-Q. Li, Y. Kawazoe, and A. Kasuya, Phys. Rev. Lett. **85**, 3440 (2000).

[106] L. Wu, H. J. Wiesmann, A. R. Moodenbaugh, R. Klie, Y. Zhu, D. O. Welch, and M. Suenaga, Phys. Rev. B **69**, 125415 (2004).

[107] W. H. Weber, K. C. Hass, and J. R. McBride, Phys. Rev. B **48**, 178 (1993).

[108] E. Mamontov, T. Egami, R. Brezny, M. Koranne, and S. Tyagi, J. Phys. Chem. B **104**, 11110 (2000).

[109] E. Mamontov and T. Egami, J. Phys. Chem. Solids **61**, 1345 (2000).

[110] R. D. Robinson, Ph.D. thesis, Columbia University, 2004.

[111] M. Kovalenko and A. Kupryazhkin, J. Nucl. Mater. **430**, 12 (2012).

[112] M. H. Dickens, M. T. Hutchings, J. Kjems, and R. E. Lechner, J. Phys. C: Solid State **11**, L583 (1978).

[113] J. Garcia-Barriocanal *et al.*, Science **321**, 676 (2008).

[114] T. J. Pennycook, M. J. Beck, K. Varga, M. Varela, S. J. Pennycook, and S. T. Pantelides, Phys. Rev. Lett. **104**, 115901 (2010).

[115] As the frequency approaches zero when the strain is increased further, anharmonic effects will become dominant. These will dampen the atomic motion and redistribute the thermal energy via phonon-phonon interactions, meaning that the amplitude will not become infinite.

[116] Interestingly, this result is counterintuitive in the context of symmetry based predictions of phase stability. Typically, one observes an increase in symmetry with temperature, or equally a decrease with pressure. With ceria, the opposite occurs according to our calculations, when vibrational free energy is not taken into account.